EUROFUSION CP(15)10/05

C. Dethloffe et al.

Microstructural Defects in EUROFER 97 after Different Neutron Irradiation Conditions

17th International Conference on Fusion Reactor Materials (ICFRM),
Aachen, Germany.
(11th October 2015 – 16th October 2015)

This work has been carried out within the framework of the EUROfusion Consortium and has received funding from the Euratom research and training programme 2014-2018 under grant agreement No 633053. The views and opinions expressed herein do not necessarily reflect those of the European Commission.

Microstructural defects in EUROFER 97 after different neutron irradiation conditions

Christian Dethloff*, Ermile Gaganidze, Jarir Aktaa

Karlsruhe Institute of Technology (KIT), Institute for Applied Materials (IAM), Hermann-von-Helmholtz-Platz 1, 76344 Eggenstein-Leopoldshafen, Germany

Abstract

Characterization of irradiation induced microstructural defects is essential for assessing the applicability of structural steels like the Reduced Activation Ferritic/Martensitic steel EUROFER 97 in upcoming fusion reactors. In this work Transmission Electron Microscopy (TEM) is used to determine the defect microstructure after different neutron irradiation conditions. In particular dislocation loops, voids and precipitates are analyzed concerning defect nature, density and size distribution after irradiation to 15 dpa at 300 °C in the mixed spectrum High Flux Reactor (HFR). New results are combined with previously obtained data from irradiation in the fast spectrum BOR-60 reactor (15 and 32 dpa, 330 °C), which allows for assessment of dose and dose rate effects on the aforementioned irradiation induced defects.

Keywords: Transmission Electron Microscopy (TEM), RAFM steels, irradiation defects, microstructural analysis

1. Introduction

Neutron irradiation induced microstructural defects deteriorate mechanical properties of structural materials. Even though reduced activation ferritic/martensitic (RAFM) steels like the European variant EUROFER 97 are especially designed for withstanding the harsh environment in future fusion reactors, they still suffer from low temperature hardening and embrittlement which limit their application. Therefore microstructural characterization of irradiation induced defects is the key for understanding irradiation effects and correlating subsequent changes in mechanical properties.

Since irradiation in a fusion like neutron spectrum is not available at present, different fission reactor irradiation experiments had been performed. Among these neutron irradiations, the SPICE experiment (300 °C, 15 dpa) [1, 2] carried out in the mixed spectrum High Flux Reactor (HFR) of NRG in Petten, and the WTZ 01/577 (330 °C, 15 dpa) [3] and ARBOR1 experiment (330 °C, 32 dpa) [4] carried out in the BOR-60 fast reactor of SSC RIAR in Dimitrovgrad are of great importance for this work (for detailed specifications of irradiation experiments see next section).

EUROFER 97 in the unirradiated reference state has been characterized concerning material and mechanical properties [5, 6] and microstructural stability under thermal annealing [7]. Irradiation influence on microstructure was determined concerning dislocation loops and voids after WTZ 01/577 and ARBOR1 [8] and after SPICE [9], and precipitates [10] after ARBOR1 irradiation. Analyses on helium bubbles were performed on boron doped [11] EUROFER 97 based steels, where boron artificially increased helium generation to a value comparable to fusion conditions, after ARBOR1 [12] and SPICE [13] irradiation. The correlation of irradiation defects with change in mechanical properties of EUROFER 97 has been recently assessed [14] making use of appropriate hardening models like the Dispersed Barrier Hardening (DBH) model [15].

In this work, new results on irradiation defects microstructure are presented. The investigation completes characterizations of different defect types concerning sizes and densities for the different irradiation experiments and addresses existing disagreement in previous publications.

2. Experimental procedure and technique

The basic material used in this work is the RAFM steel EUROFER 97 (rolled plate material, heat 83697) produced by Böhler Austria GmbH with a composition of 8.91 Cr 1.08 W 0.48 Mn 0.20 V 0.14 Ta 0.006 Ti 0.12 C (wt.%, Fe balance) [16]. The material was delivered in a normalized (980 °C for 0.5 h) and tempered (760 °C for 1.5 h) condition. Several types of mechanical testing specimens were neutron irradiated in the irradiation experiments SPICE, WTZ 01/577 and ARBOR1: the corresponding irradiation specifications are shown in Tab. 1.

TEM samples were manufactured in the Hot Cells at the Fusion Materials Laboratory (FML) of KIT from undeformed parts of irradiated EUROFER 97 impact test specimens with a cross-sectional area of $3 \times 4\,mm^2$. By using a cutting wheel slices with thicknesses of about 150-200 µm were prepared and subjected to electrolytic polishing in a solution of 20% H_2SO_4 + 80% CH_3OH at room temperature with a Tenupol-5 jet polisher. Afterwards, in order to minimize radioactivity and also the influence of the magnetic sample on the electron beam, discs of only 1 mm in diameter including the electron-transparent region were punched out. A foldable copper net carried the 1 mm sample and was used for examination in the TEM.

*Corresponding author.
Email address: christian.dethloff@kit.edu (Christian Dethloff)
URL: http://www.iam.kit.edu/wbm (Christian Dethloff)

Table 1: Specifications of irradiation experiments. Detailed information can be found in [1, 2, 3, 4].

experiment	SPICE	WTZ 01/577	ARBOR1
irradiation facility	HFR Petten	BOR-60	BOR-60
dose (dpa)	15	15	32
neutron flux (E>0.1 MeV) ($m^{-2}s^{-1}$)	4.0×10^{18}	1.8×10^{19}	1.8×10^{19}
neutron flux (thermal) ($m^{-2}s^{-1}$)	1.4×10^{18}	–	–
irradiation temp. (°C)	300	330	330

TEM investigations were performed at 200 kV on a high resolution FEI Tecnai G^2 F20 X-TWIN microscope equipped with a post-column GIF Tridiem energy filter and located in the Hot Cells at FML. Prior to each investigation the surface contamination of the TEM specimens was reduced by applying a plasma cleaning treatment of 10 min with air plasma. In TEM mode, all images were recorded with the GIF camera and zero-loss filtered with an energy slit of 15 eV to improve contrast. In scanning TEM (STEM), nanoprobe mode was used resulting in a probe diameter of approximately 1.5 nm, and images were processed by a High Angle Annular Dark-Field (HAADF) detector. Elemental analysis by Energy Dispersive X-ray spectroscopy (EDX) was performed. For defect density evaluation the foil thickness of the investigated regions was determined by Convergent Beam Electron Diffraction (CBED) [17, 18], and the recorded CBED patterns were analyzed using a DigitalMicrograph^{TM} script [19].

3. Results

3.1. Dislocation loops

The weak-beam dark-field (WBDF) technique [20] is used for imaging dislocation loops. The diffraction conditions, as given in Tab. 2, were chosen in such a way that an excitation error s_g of approximately 0.2 nm^{-1} was achieved. This allows for imaging of small defects down to 1 nm of size, since the diffraction contrast can be minimized and approaches to the real physical size of the dislocation loops. Fig. 1 shows a WBDF image of area 2 of SPICE specimen SPI-1 with diffraction conditions given in the figure caption. In the image enlargement some dislocation loops are marked by circles. Due to the invisibility criterion $g \cdot b = 0$ only a fraction of dislocation loops are visible. Therefore different diffraction conditions are analyzed as shown in Tab. 2, the table also gives the invisible loop types for each condition.

Dislocation loop size distributions with a histogram bin size of 1 nm for alle three diffraction conditions are presented in Fig. 2. Analyses for g = {3-10} and {200} show comparable dislocation loop size distributions. A peak around 3 nm is observed, with a small amount of larger loops exceeding 8 nm. The analysis for g = {2-11} differs however, since a much higher fraction of smallest loops below 2 nm is observed.

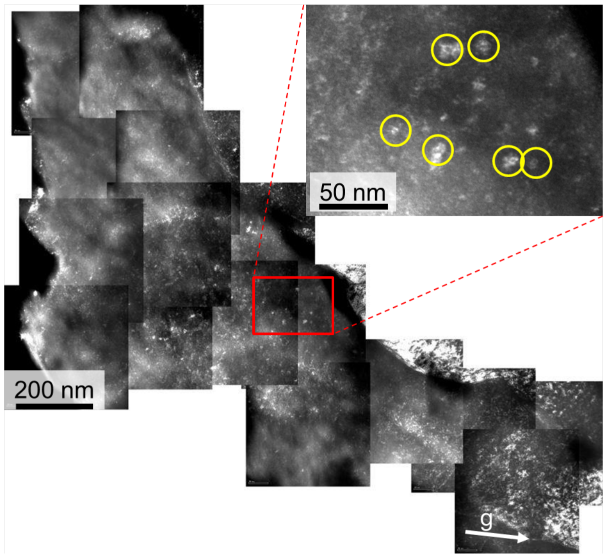

Figure 1: TEM-WBDF micrograph showing investigated area 2 of sample SPI-1 after 15 dpa at 300°C. The WBDF images are taken near a [011] zone axis with $g(3.1g)$, g = {2-11}. The red marked area is shown enlarged to visualize dislocation loops.

Corresponding densities and mean diameters of visible dislocation loops are given in Tab. 2. Although identification and measurement of smallest loops is more difficult due to limited TEM resolution, results indicate that in general loops of type $\frac{1}{2}\langle 111\rangle$ are larger in size and less numerous than loops of type $\langle 100\rangle$ when taking into account the respectively visible loop types. The actual loop densities, despite the partial invisibility, can be estimated by solving a set of linear equations as proposed in [21]. Results give a dislocation loop density of $N_{\langle 100\rangle} = 4.9 \times 10^{21}$ m^{-3} and $N_{\frac{1}{2}\langle 111\rangle} = 1.4 \times 10^{21}$ m^{-3}, i.e. in total $N_{tot} = 6.3 \times 10^{21}$ m^{-3}.

3.2. Voids

Voids are identified and made visible by performing TEM bright-field (BF) through-focal series. From under- to overfo-

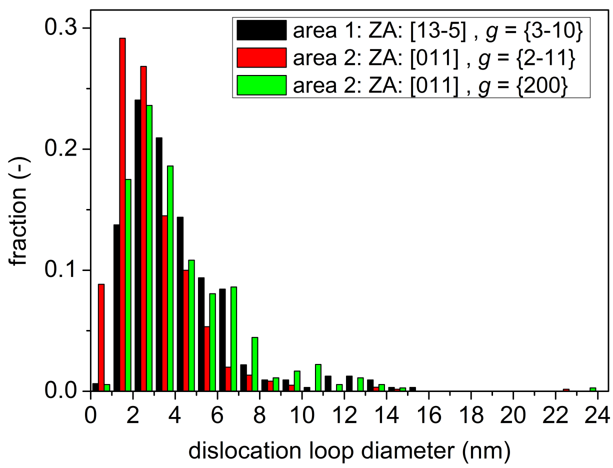

Figure 2: Dislocation loop size distributions of sample SPI-1 after 15 dpa at 300°C for different diffraction conditions (see also Tab. 2).

Table 2: Dislocation loop analysis of sample SPI-1 after 15 dpa at 300°C.

	zone axis ZA	g	diffraction condition	invisible loop types, b	foil thickness (nm)	density (m^{-3})	mean diameter (nm)
area 1	[13-5]	{3-10}	$g(3.1g)$	⟨001⟩	135	5.1×10^{21}	4.1
area 2	[011]	{2-11}	$g(3.1g)$	$\frac{1}{2}$⟨11-1⟩	151	5.8×10^{21}	2.8
area 2	[011]	{200}	$g(3.1g)$	⟨010⟩, ⟨001⟩	151	2.8×10^{21}	4.2

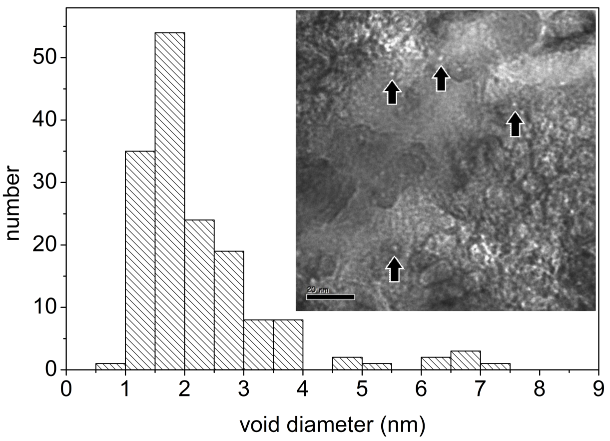

Figure 3: Void size distributions of sample SPI-1 after 15 dpa at 300°C. TEM BF underfocused image (-1 µm) examplarily shows voids with bright interior contrast.

cus, the diffraction contrast of voids changes from bright interior to dark, while the fresnel fringes change contrast vice versa [22]. Fig. 3 shows the void size distribution after 15 dpa at 300°C in sample SPI-1. In the overlay voids can be observed in underfocus condition with a focus of -1 µm. Voids are homogeneously distributed in the matrix after irradiation, no preferential nucleation sites are observed. Mean void diameter is 2.3 nm, the void density is determined as 6.3×10^{21} m^{-3}.

3.3. Precipitates

Precipitates in sample SPI-1 are analyzed by STEM making use of the high Z contrast of the HAADF detector. The analysis in this section is following the investigation approach in [10]. Precipitate types are identified by EDX, and their size is determined by calculating an equivalent precipitate diameter from their cross-sectional area [23].

In Fig. 4a, a part of the whole investigated area of sample SPI-1 was analyzed both by EDX and size. Precipitates can be distinguished between Ta and V enriched MX types, and $M_{23}C_6$ type enriched in both Cr and W. Precipitates which could not be assigned to the mentioned types are declared as "not clear". For the most part, small Ta rich MX and large $M_{23}C_6$ type precipitates are observed. Total precipitate size distribution is described by two log-normal distributed fitting curves of type $f(x) = A/(\sqrt{2\pi}\sigma x)\exp[-(\ln(x/\overline{d}))^2/(2\sigma^2)]$ with separate mean diameter $\overline{d}$, standard deviation σ and curve integral A. Fitting values for the MX ($M_{23}C_6$) size distribution are $\overline{d}$ = 26 (83) nm, σ = 0.35 (0.45), A = 4.8 (5.9). Recalculating the continuous fitting curves into discrete histogram values (see [10]) yield a mean precipitate diameter of 27 nm for MX and 91 nm for $M_{23}C_6$, with a MX number fraction of 46%. With a mean foil thickness of 151 nm, the total precipitate density is determined as 7.9×10^{19} m^{-3}. Thus the precipitate volume fraction after SPICE irradiation in EUROFER 97 can be estimated to 1.08%.

4. Discussion

In this section latest results on microstructural defects from this work are compared to our previously determined findings from WTZ 01/577 and ARBOR1 irradiation [8, 10]. Fig. 5 shows summarized data, which will be discussed in the following sections for each defect type in detail including further results from literature.

In general TEM is most suitable to visualize smallest microstructural defects down to a size in the range of nanometers. That is, however, the analysis of smallest defects leads to a very small investigated sample volume and thus limited statistics especially when dealing with small defect densities. This problem is even intensified when defects are not homogeneously distributed in the sample but located at preferential sites e.g. at grain boundaries as in the case of precipitates (see below).

4.1. Dislocation loops

For a appropriate comparison densities of visible dislocation loops from [8] were recalculated to total loop densities according to [21] as described in the previous section. The dislocation loop density increases with both irradiation dose and dose rate, when data in Fig. 5a is compared between 15 dpa and 32 dpa in BOR-60, and 15 dpa in HFR and BOR-60, respectively. The mean loop diameter in Fig. 5b at 15 dpa in HFR and BOR-60 is comparable, while in BOR-60 an increase is observed from 15 to 32 dpa. The dislocation loop density seems to be more sensitive to the dose rate, while loop sizes show a higher dependence on irradiation dose.

Further investigations on dislocation loops in EUROFER 97 after 15 dpa at 300 °C in HFR were reported in [9]. Results show a comparable loop density of 4×10^{21} m^{-3}, the mean diameter, however, was determined to be 14 nm. It was stated that only loops were counted that could be clearly identified. In our work and the previous one [8] loop size distributions are observed differently. Although a small fraction of loops are in the size regime between 10 and 15 nm, the largest fraction is between 1 and 7 nm. Although the smallest loops are more difficult to indentify, also in our work only loops were counted

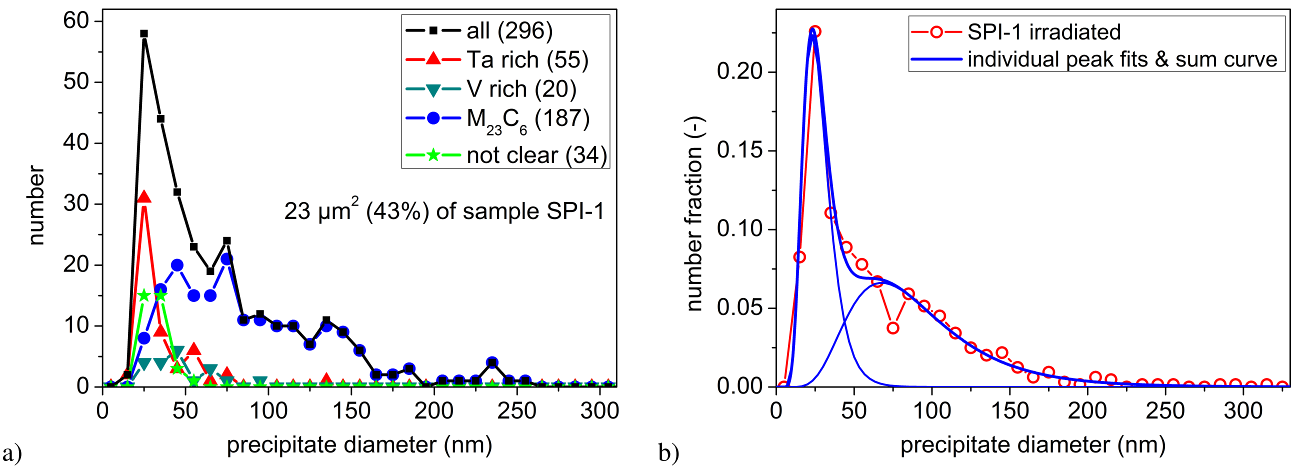

Figure 4: Precipitate size distributions in sample SPI-1. a) Histograms of precipitates are analyzed by EDX and evaluated with respect to size. Small Ta rich MX and large $M_{23}C_6$ type precipitates are mainly observed. b) For the whole investigated area the precipitate histogram was fitted by two log-normal distributions according to mainly observed MX and $M_{23}C_6$ precipitates analog to [10].

which could be recognized as such. For that reason, the magnification and resolution of the TEM images was chosen to be high, to observe also the smallest visible loops.

4.2. *Voids*

The comparison of void densities after different irradiation conditions can be observed in Fig. 5a. It is noteworthy that after 15 dpa in HFR the void density is increased by a factor of 20 when compared to 15 dpa in BOR-60. The void density even reaches the value of the dislocation loop density after 15 dpa in HFR. What at first seems inconclusive, can be explained by considering not only dose and dose rate properties, but also the amount of helium gas, which is produced differently under thermal neutrons in HFR and fast neutron in BOR-60. It was estimated in [24] that after 15 dpa in HFR 10.2 atomic parts per million (appm) helium is generated in EUROFER 97 by transmutation of steel matrix elements through interaction with thermal neutrons, while fast neutrons from BOR-60 produce almost no helium. The image contrast of voids and helium filled cavities in TEM is identical, that means they can not be easily distinguished. What is well known and for example described in [25], even small amounts of helium stabilize vacancy clusters and enhance void nucleation, and therefore can explain a much higher void density under HFR irradiation.

A comparison of the mean void diameter between 15 and 32 dpa after BOR-60 irradiation indicates a decrease of void size with dose while at the same time the density increases by a factor of six. When analyzing the results from [8] more closely, statistics for voids after 15 dpa in BOR-60 were especially poor with only 31 voids detected in the investigated sample volume. Results for 32 dpa after BOR-60 are more reliable since in this case at least 112 voids were observed and measured. One can assert that even in the case of defects with a number density of about $10^{20}\,m^{-3}$ like it is for voids after 15 dpa after BOR-60, statistics of size distributions derived by TEM are very poor, and thus a large volume of the TEM sample has to be investigated to diminish that drawback. It is this poor statistics which apparently leads to the large error in the mean void diameter determination after 15 dpa in BOR-60.

Results from Small Angle Neutron Scattering (SANS) experiments on HFR (16 dpa, 250°C) and BOR-60 (32 dpa, 330°C) specimens also indicate a large density of microvoids [26] under HFR irradiation conditions, with a volume fraction twice as high as for the BOR-60 sample. Although absolute values differ the tendency is comparable to present TEM results. Since SANS is a volume analysis technique it eliminates the TEM drawback of a small investigation volume and aforementioned limited statistics. However, identification of different irradiation defects is not as straightforward as in TEM, and is mainly related to the different defect size ranges and defect specific neutron contrast.

4.3. *Precipitates*

The comparison of mean precipitate diameters in Fig. 5c for the given irradiation conditions indicate a clear increase of defect size with dose for both MX and $M_{23}C_6$ types. Note that the investigation after irradiation to 15 dpa at BOR-60 is not yet completed. Results on precipitate densities are not so straighforward as shown in Fig. 5a. As mentioned before, a low defect density and preferential precipitation (at least of $M_{23}C_6$) at grain boundaries in combination with a large range of precipitate diameters from 9 to 330 nm lead to poor statistics and highest inaccuracy in determined precipitate densities of all defect types. That can also be observed in the large variation of the MX number fraction between 30 and 46 % in the different investigated samples. Therefore changes in precipitate densities have to be regarded rather insignificant, and irradiation is more likely causing the growth of pre-existing precipitates from the manufacturing process. The estimation of the total precipitate volume fraction shows an increase with irradiation dose as shown in Fig. 5d. Irradiation induced precipitation is expected by thermodynamics, because the steel matrix is not in a state of equilibrium [27], precipitation is kinetically hindered. However, it remains unclear if chromium rich α' precipitates [28]

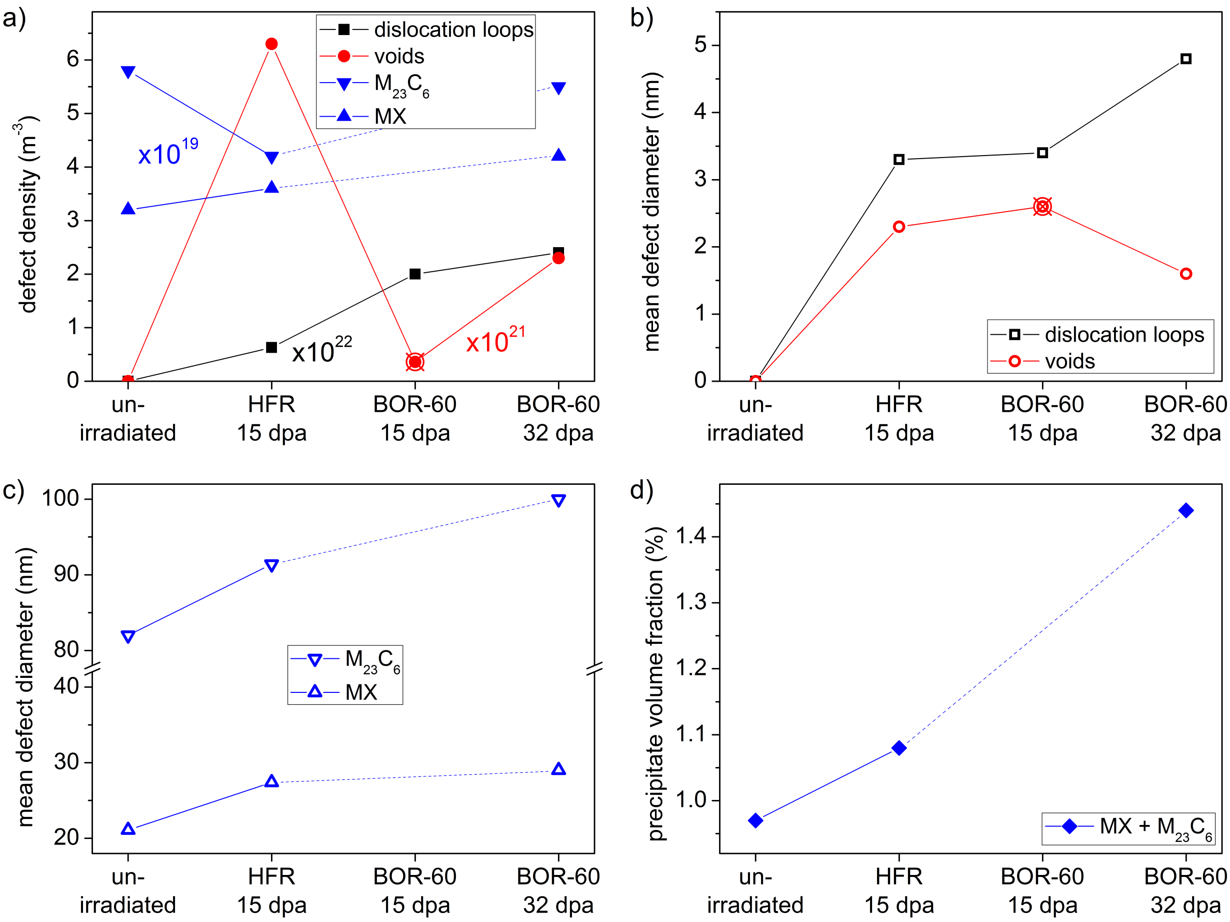

Figure 5: Summary of microstructural investigations on irradiation defects and comparison for different irradiation conditions from this work and [8, 10]. Defect densities are summarized in a) with dimensions as indicated. Defect sizes are shown in b) and c), the estimated precipitate volume fraction is given in d). Note that the investigation on precipitates for 15 dpa in BOR-60 is still in progress. Results for voids after 15 dpa at BOR-60 are less reliable (indicated by the crossed circles) as it is discussed in the respective paragraph.

can form in 9 wt.% chromium EUROFER 97 after neutron irradiation, since they have not been observed by TEM so far.

Atom Probe Tomography (APT) investigations [29] on EUROFER 97 after BOR-60 irradiation (32 dpa, 330°C) identified nanometer sized (3 to 4 nm) Cr and Mn rich segregations with a high volume density of $5 \times 10^{24}\,m^{-3}$. Although they could not be related to α′, the authors state they could be initial stages of α′ and other carbides. The impact of these small clusters on hardening remains unclear, but since the segregations are described as diffuse they are not supposed to have a strong influence when compared to e.g. dislocation loops. Nevertheless, at the observed high density these segregations may have noticable effect on the yield stress as discussed in [30].

5. Conclusions

In this work an investigation has been performed of dose and dose rate effects on irradiation induced defects in EUROFER 97 after neutron irradiation in HFR and BOR-60. The nature of defects and their size distributions have been determined by means of TEM and a comparison of results from irradiation programs SPICE, WTZ 01/577 and ARBOR1 were presented. The following conclusions can be drawn.

- Dislocation loops of type $\langle 100 \rangle$ are observed more frequently than type $\frac{1}{2}\langle 111 \rangle$ after HFR irradiation. Loop density steadily increases with dose and dose rate, mean loop size increases mainly with dose.
- Voids show a homogeneous spatial distribution after HFR and BOR-60 irradiation in the temperature range between 300 and 330°C. A high volume fraction of voids is observed after mixed spectrum HFR irradiation, which can be related to stabilizing effects of simultaneous helium gas production on void nucleation.
- Precipitates of types MX and $M_{23}C_6$ are observed in EUROFER 97, which show a clear growth with dose due to neutron irradiation. The precipitate volume fraction steadily increases, while possible chromium rich α′ precipitates have not been observed by TEM so far.

The comparison of different TEM investigations on irradiation defects made it obvious that results have to be assessed very carefully to avoid misleading interpretation of data especially for defects with low number density.

Further TEM investigations will focus on dose rate effects on the precipitate microstructure and identification of possible α' precipitates. Irradiation induced segregation will further be addressed.

Acknowledgments

R. Rolli and his work group of the Fusion Materials Laboratory of KIT is acknowledged for support, handling and cutting of active impact specimens in the Hot Cells.

This work has been carried out within the framework of the EUROfusion Consortium and has received funding from the Euratom research and training programme 2014-2018 under grant agreement No 633053. The views and opinions expressed herein do not necessarily reflect those of the European Commission.

References

[1] E. Gaganidze, B. Dafferner, H. Ries, R. Rolli, H. C. Schneider, J. Aktaa, FZKA 7371 (2008).
[2] E. Materna-Morris, A. Möslang, R. Rolli, H.-C. Schneider, Journal of Nuclear Materials 386-388 (2009) 422–425.
[3] C. Petersen, J. Aktaa, E. Diegele, E. Gaganidze, R. Lässer, E. Lucon, E. Materna-Morris, A. Möslang, A. Povstyanko, V. Prokhorov, J. Rensman, B. van der Schaaf, H.-C. Schneider, 21st IAEA Fusion Energy Conf., Chengdu, China, October 16-21, FT/1-4Ra (2006).
[4] C. Petersen, V. Shamardin, A. Fedoseev, G. Shimansky, V. Efimov, J. W. Rensman, Journal of Nuclear Materials 307-311 (2002) 1655–1659.
[5] R. Lindau, M. Schirra, Fusion Engineering and Design 58–59 (2001) 781–785.
[6] M. Rieth, M. Schirra, A. Falkenstein, P. Graf, S. Heger, H. Kemp, R. Lindau, H. Zimmermann, FZKA 6911 (2003) 1–83.
[7] P. Fernández, M. Garca-Mazarío, A. M. Lancha, J. Lapeña, Journal of Nuclear Materials 329–333 (2004) 273–277.
[8] O. J. Weiß, E. Gaganidze, J. Aktaa, Journal of Nuclear Materials 426 (2012) 52–58.
[9] M. Klimenkov, E. Materna-Morris, A. Möslang, Journal of Nuclear Materials 417 (2011) 124–126.
[10] C. Dethloff, E. Gaganidze, J. Aktaa, Journal of Nuclear Materials 454 (2014) 323–331.
[11] E. Materna-Morris, M. Klimenkov, A. Möslang, Materials Science Forum 730-732 (2013) 877–882.
[12] E. Gaganidze, C. Dethloff, O. J. Weiß, V. Svetukhin, M. Tikhonchev, J. Aktaa, Journal of ASTM International: Effects of Radiation on Nuclear Materials 25 (2012) 123–142.
[13] M. Klimenkov, A. Möslang, E. Materna-Morris, H.-C. Schneider, Journal of Nuclear Materials 442 (2013) S52–S57.
[14] E. Gaganidze, J. Aktaa, Fusion Engineering and Design 88 (2013) 118–128.
[15] G. E. Lucas, Journal of Nuclear Materials 206 (1993) 287–305.
[16] E. Gaganidze, H.-C. Schneider, B. Dafferner, J. Aktaa, Journal of Nuclear Materials 355 (2006) 83–88.
[17] P. M. Kelly, A. Jostsons, R. G. Blake, J. G. Napier, Phys. Status Solidi (a) 31 (1975) 771–780.
[18] S. M. Allen, Philosophical Magazine A 43 (1981) 325–335.
[19] V. Hou, Microscopy and Microanalysis 10 (2004) 1380–1381.
[20] D. J. H. Cockayne, I. L. F. Ray, M. J. Whelan, Philosophical Magazine 20 (1969) 1265–1270.
[21] A. Prokhodtseva, B. Décamps, A. Ramar, R. Schäublin, Acta Materialia 61 (2013) 6958–6971.
[22] M. L. Jenkins, Journal of Nuclear Materials 216 (1994) 124–156.
[23] Y. Qin, G. Götz, W. Blum, Z. G. Zhu, Journal of Alloys and Compounds 352 (2003) 260–264.
[24] C. Dethloff, E. Gaganidze, V. V. Svetukhin, J. Aktaa, Journal of Nuclear Materials 426 (2012) 287–297.
[25] S. J. Zinkle, W. G. Wolfer, G. L. Kulcinski, L. E. Seitzman, Philosophical Magazine A 55 (1987) 127–140.
[26] R. Coppola, E. Gaganidze, M. Klimenkov, C. Dethloff, R. Lindau, M. Valli, J. Aktaa, A. Möslang, Nuclear Materials and Energy (*to be published*). 17th International Conference on Fusion Reactor Materials, Aachen, Germany, October 2015.
[27] R. L. Klueh, K. Shiba, M. A. Sokolov, Journal of Nuclear Materials 377 (2008) 427–437.
[28] L. Malerba, A. Caro, J. Wallenius, Journal of Nuclear Materials 382 (2008) 112–125.
[29] S. V. Rogozhkin, A. A. Nikitin, A. A. Aleev, A. B. Germanov, A. G. Zaluzhnyi, Inorganic Materials: Applied Research 4 (2013) 112–118.
[30] D. Terentyev, B. Minov, D. Song, H. Duan, M. Konstantinovic, Nuclear Materials and Energy (*to be published*). 17th International Conference on Fusion Reactor Materials, 2015.